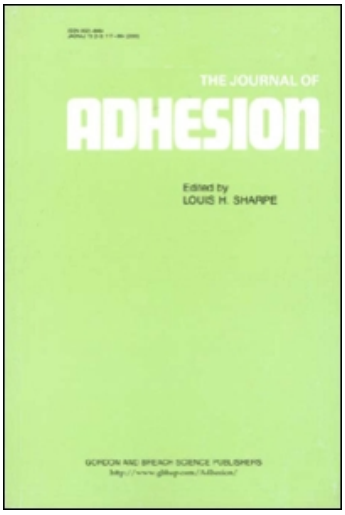

The Journal of Adhesion
Publication details, including instructions for authors and subscription information:
http://www.informaworld.com/smpp/title~content=t713453635

Comparison of Analytical, Numerical, and Experimental Methods in Deriving Fracture Toughness Properties of Adhesives Using Bonded Double Lap Joint Specimens

A. R. Setoodeh[a]; H. Hadavinia[b]; F. R. Biglari[c]; K. Nikbin[d]
[a] Mechanical Engineering Department, Imperial College London, South Kensington Campus, United Kingdom and Mechanical Engineering Department, School of Engineering, Ferdowsi University, Mashhad, Iran [b] School of Engineering, Kingston University, London, United Kingdom [c] Mechanical Engineering Department, Amirkabir University of Technology, Tehran, Iran [d] Mechanical Engineering Department, Imperial College London, South Kensington Campus, United Kingdom

To cite this Article Setoodeh, A. R. , Hadavinia, H. , Biglari, F. R. and Nikbin, K.(2005) 'Comparison of Analytical, Numerical, and Experimental Methods in Deriving Fracture Toughness Properties of Adhesives Using Bonded Double Lap Joint Specimens', The Journal of Adhesion, 81: 5, 529 — 553
To link to this Article: DOI: 10.1080/00218460590944963
URL: http://dx.doi.org/10.1080/00218460590944963

The Journal of Adhesion, 81:529–553, 2005

ISSN: 0021-8464 print/1545-5823 online
DOI: 10.1080/00218460590944963

Taylor & Francis
Taylor & Francis Group

Comparison of Analytical, Numerical, and Experimental Methods in Deriving Fracture Toughness Properties of Adhesives Using Bonded Double Lap Joint Specimens

A. R. Setoodeh
Mechanical Engineering Department, Imperial College London, South Kensington Campus, United Kingdom and
Mechanical Engineering Department, School of Engineering, Ferdowsi University, Mashhad, Iran

H. Hadavinia
School of Engineering, Kingston University, London, United Kingdom

F. R. Biglari
Mechanical Engineering Department, Amirkabir University of Technology, Tehran, Iran

K. Nikbin
Mechanical Engineering Department, Imperial College London, South Kensington Campus, United Kingdom

Stress and fracture analysis of bonded double lap joint (DLJ) specimens have been investigated in this paper. Numerical and analytical methods have been used to obtain shear- and peel-stress distributions in the DLJ. The generalized analytical solution for the peel stress was calculated for various forms of the DLJ geometry and, by using crack closure integral (CCI) and by means of the J-integral approach, the analytical strain energy-release rate, G, was calculated. Experimental fracture tests have also been conducted to validate the results. The specimens were made of steel substrates bonded by an adhesive and loaded under tension. Specimens with cracks on both sides and at either end of the DLJ interface were tested to compare the fracture behavior for the two crack positions where tensile and compressive peel stresses exist. Tests confirmed that the substrates essentially behave elastically. Therefore, a linear elastic solution for the bonded region of the DLJ was developed. The fracture energy parameter, G, calculated from the elastic experimental compliance for different crack lengths, was compared with numerical and analytical calculations using the experimental fracture loads.

Received 5 July 2005; in final form 23 January 2005.
Address correspondence to K. Nikbin, Mechanical Engineering Department, Imperial College London, Exhibition Road, London SW7 2AZ, UK. E-mail: k.nikbin@ic.ac.uk

The stresses from analytical analysis were also compared with those from the finite element results. The strain energy-release rate for fracture, G_f, for the adhesive has been shown to have no R-curve resistance, was relatively independent of crack length, and compared well with those obtained from numerical and analytical solutions. However, it was found that fracture energy for the crack starter in the position where the peel stress was tensile was about 20% lower than where the crack was positioned at the side, where the peel stress was found to be compressive.

Keywords: Fracture toughness; Compliance method; Double lap joint; Adhesive

INTRODUCTION

Adhesive joints are widely used as the principal alternative to conventional mechanical fasteners such as screws, rivets, and bolts in industry as well as for insulating applications. The basic reasons for this special attention to adhesive joints can be seen in some key points, such as uniform load transfer, removal of any discontinuities in the geometry, and reduction of the weight of the structure. These design process require that the stress field in the bonded region both in an uncracked and a cracked condition be precisely estimated. In addition, it should be able to predict by the aid of a failure criterion or a fracture mechanics criterion, the strength and durability of bonded joint under static or cyclic loading.

The objective of the present article is to derive a simplified analytical solution for a generic DLJ geometry and validate it with numerical and experimental work. Hence, a short review of related previous work is presented here. There are a number of analytical solutions for stress distribution in the lap joint geometry. Different assumptions and simplifications have been made to reach these solutions. Volkersen [1] made the first attempt to show the elastic behavior of the adhesive layer of DLJs, which were subjected to a tensile loading. Goland and Reissner [2] considered cemented single lap joints. Hart-Smith [3] developed a more practical modeling for DLJs. He derived an explicit analytical solution for the static load-carrying capacity of double lap adhesively bonded joints and extended the elastic solution of Volkersen, which accounted for only imbalance stiffness. Hart-Smith derived both shear- and peel-stress distributions while he made some simplifications for uncoupling shear and peel stresses. He also derived the solutions for single lap joints [4] and stepped lap joints [5]. Williams [6] produced a general method for the calculation of energy-release rates for cracked laminates. Kinloch [7] presented a shear-lag model that took into account the shear deformation of the adhesive layer. Hamoush and Ahmad [8] developed a criterion for

estimating the interface-separation load for adhesive joints of two dissimilar materials using a fracture mechanics approach. Bigwood and Crocombe [9] developed an elastic analysis for adhesively bonded single lap joints. Fernlund and Spelt [10] presented an analytical method for calculating adhesive-joint fracture parameters using the *J*-integral method. Edde and Verreman [11] derived an analytical solution of shear and peel stresses for the case of clamped and similar adherends using a beam theory as suggested by Goland and Reissner. Chiu and Jones [12] presented a numerical study of a thick adherend lap joint and a symmetrical DLJ, in which they discussed the effect of varying adherend and adhesive thicknesses on the stress distribution in the thin adhesive layer. Williams [13] determined the energy-release rates for uniform strips in tension and bending. Hadavinia *et al*. [14] used CCI and *J*-integral methods to calculate the strain energy-release rate in bonded single lap joints. Lee [15] studied nonlinear behavior of tapered bonded joints and concluded that tapered joints are efficient because of the reduction in peel stress at the adherend tips. Her [16] presented an analytical solution for stress analysis of adhesively bonded lap joints using a simplified one-dimensional model based on classical elasticity theory. Pereira and Morais [17] conducted an experimental study on the strength of adhesively bonded stainless steel joints, prepared with epoxy and acrylic adhesives, and measured Mode I critical strain energy-release rate.

MODELING OF DOUBLE LAP JOINT

In this article, the focus is on the double lap joint (DLJ) as a special case. However, the presented method can easily be extended to the analysis of a single lap joint. The DLJs were made from an epoxy adhesive used to bond the steel substrates. A schematic of a double lap joint specimen is shown in Figure 1. The outer adherends have

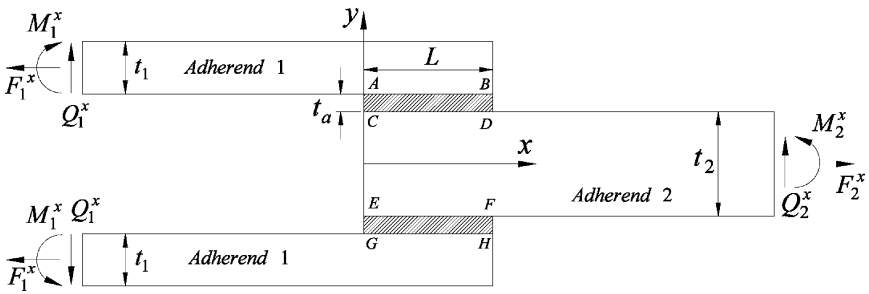

FIGURE 1 The schematic drawing of a double lap joint (DLJ) geometry and its loading.

a Young's modulus E_1, shear modulus G_1, Poisson's ratio ν_1, and thickness t_1, whereas E_2, G_2, ν_2, and t_2 are Young's modulus, shear modulus, Poisson's ratio, and thickness of inner adherend, respectively. The joint overlap length is L and width is w, whereas E_a, G_a, ν_a, and t_a are Young's modulus, shear modulus, Poisson's ratio, and thickness of the adhesive layer, respectively. The double lap joint can be loaded in tension (compression), F^x, and shear, Q^x, as well as moment, M^x, at the substrates' ends, where the superscript x refers to all external loads applied in a plane normal to x-axis (see Figure 1).

ANALYTICAL SOLUTION

The classical theory of plates is employed to develop the differential equations that describe the shear and peel stresses along the bondline. The procedure is general and can be easily used in different situations. Figure 2 shows a free-body diagram of an element of a DLJ in the bonded region. The substrates are considered to behave as linear elastic cylindrically bent plates. It was assumed that the plate behaves in plane stress condition in the x–z plane and in plane strain condition in the x–y plane. In this section, the general and simplified solutions of shear- and peel-stress distribution along the bondline is discussed using the equilibrium equations of the inner and the outer adherends presented in Appendix A.

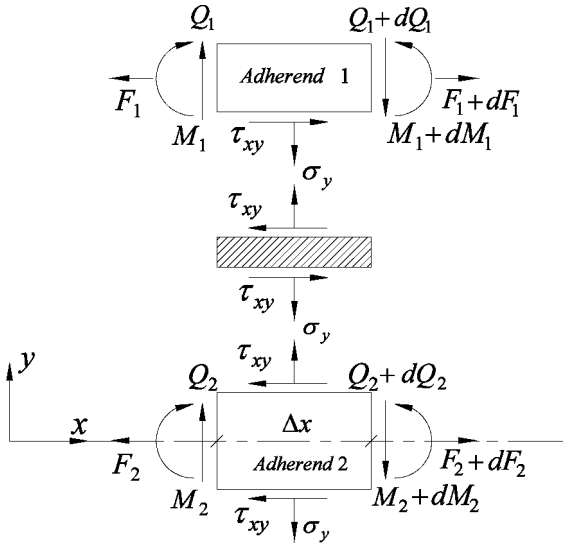

FIGURE 2 Free-body diagram of a double lap joint element showing the detail in the bonded region.

General Solution

The shear strain in the adhesive can be taken as relative displacements of the upper (u_1) and lower layers (u_2) in the x direction, which are in contact with the substrates. Thus, assuming elastic behavior, the shear stress can be written as

$$\tau_{xy} = \frac{G_a}{t_a}(u_2 - u_1) \tag{1}$$

where u is the displacement in the x direction. As presented in Figure 2 and under the assumptions made for the state of stress and strain, the component of strains resulting from longitudinal and moment loading for the two adherends can be superimposed to obtain the relations

$$\frac{du_1}{dx} = n_1\left(F_1 + \frac{6M_1}{t_1}\right), \quad \frac{du_2}{dx} = n_2\left(F_2 - \frac{6M_2}{t_2}\right) \tag{2}$$

in which subscripts 1 and 2 stand for the outer and the inner adherends, respectively, and

$$n_i = \frac{1 - \nu_i^2}{E_i t_i}, \quad i = 1, 2.$$

Differentiating Equation (1) and substituting from Equation (2) lead to the following equation:

$$\frac{d\tau_{xy}}{dx} = \frac{G_a n_2}{t_a}\left[(F_2 - \phi F_1) - \frac{6}{t_2}\left(M_2 + \frac{\phi t_2}{t_1}M_1\right)\right], \quad \phi = \frac{n_1}{n_2}. \tag{3}$$

Two further differentiations from Equation (3) and substitutions of appropriate equations from Appendix A for moment and longitudinal and transverse forces yield

$$\frac{d^2\tau_{xy}}{dx^2} = \frac{G_a n_2}{t_a}\left[(2 + 4\phi)\tau_{xy} - \frac{6}{t_2}\left(Q_2 + \frac{\phi t_2}{t_1}Q_1\right)\right] \tag{4}$$

$$\frac{d^3\tau_{xy}}{dx^3} - \frac{G_a n_2}{t_a}\left[(2 + 4\phi)\frac{d\tau_{xy}}{dx} + \frac{6\phi}{t_1}\sigma_y\right] = 0. \tag{5}$$

Equation (5) is a differential equation in which shear stress, τ_{xy}, and peel stress, σ_y, are coupled. The shear- and peel-stress distributions can be found by deriving another differential equation, and then the shear stress can be uncoupled from the peel stress.

Hooke's law for the case of plane stress linear elastic cylindrically bent plates is used to evaluate the relation between the bending moment intensity (per unit width) and deformation in the y direction [18] as

$$\frac{d^2 \mathrm{v}_i}{dx^2} = -\frac{M_i}{D_i}, \quad D_i = \frac{E_i t_i^3}{12(1-\nu_i^2)}, \quad i = 1, 2. \tag{6}$$

in which D_i is the bending rigidity of the substrates.

The elastic peel stress shown in Figure 2 is defined as

$$\sigma_y = -\frac{E_a}{t_a}(\mathrm{v}_2 - \mathrm{v}_1). \tag{7}$$

By taking the second to the fourth derivatives of Equation (7) and, after substitution of equilibrium relations from Appendix A, the following differential equations are obtained:

$$\frac{d^2\sigma_y}{dx^2} = \frac{E_a}{t_a D_2}(M_2 - fM_1), \quad f = \frac{D_2}{D_1}, \tag{8}$$

$$\frac{d^3\sigma_y}{dx^3} = \frac{E_a}{t_a D_2}\left(Q_2 - fQ_1 + \frac{ft_1}{2}\tau_{xy}\right), \tag{9}$$

and

$$\frac{d^4\sigma_y}{dx^4} - \frac{E_a}{t_a D_1}\left(\sigma_y + \frac{t_1}{2}\frac{d\tau_{xy}}{dx}\right) = 0. \tag{10}$$

It can be seen that, in the fourth-order differential equation, the normal and the shear stresses are again coupled; therefore, stress distributions cannot be found directly. The stress field can be found by solving Equations (5) and (10) simultaneously to separate the variables. After some manipulations and rearrangements, the following two uncoupled seventh- and sixth-order differential equations in terms of a nondimensional parameter, $\xi = x/L$, are derived:

$$\frac{d^7\tau_{xy}}{d\xi^7} - k_\tau^2\frac{d^5\tau_{xy}}{d\xi^5} - 4k_\sigma^4\frac{d^3\tau_{xy}}{d\xi^3} + 4k_\tau^2 k_\sigma^4\left(1 - \frac{3\phi}{2+4\phi}\right)\frac{d\tau_{xy}}{d\xi} = 0, \tag{11}$$

$$\frac{d^6\sigma_y}{d\xi^6} - k_\tau^2\frac{d^4\sigma_y}{d\xi^4} - 4k_\sigma^4\frac{d^2\sigma_y}{d\xi^2} + 4k_\tau^2 k_\sigma^4\left(1 - \frac{3\phi}{2+4\phi}\right)\sigma_y = 0, \tag{12}$$

where

$$k_\tau^2 = (2 + 4\phi)\frac{G_a n_2 L^2}{t_a}, \quad k_\sigma^4 = \frac{E_a L^4}{4 t_a D_1}. \tag{13}$$

The solution to Equations (11) and (12) is of the form $Ae^{r\xi}$. These differential equations can be solved in the same way because the auxiliary equation is identical in both cases. The general form of shear and peel stresses is provided according to the auxiliary Equation (14) under the condition that two roots of it are real (r_1,r_2) and the third root is imaginary (r_3):

$$R^3 - k_\tau^2 R^2 - 4k_\sigma^4 R + 4k_\tau^2 k_\sigma^4 \left(1 - \frac{3\phi}{2 + 4\phi}\right) = 0, \quad R = r^2. \tag{14}$$

Of course, there is a zero root for the shear differential equation. The general form of stress distributions are

$$\begin{aligned}\tau_{xy} = {} & a_1 \sinh(r_1\xi) + a_2 \cosh(r_1\xi) + a_3 \sinh(r_2\xi) + a_4 \cosh(r_2\xi) \\ & + a_5 \sin(r_3\xi) + a_6 \cos(r_3\xi) + a_7\end{aligned} \tag{15}$$

and

$$\begin{aligned}\sigma_y = {} & b_1 \sinh(r_1\xi) + b_2 \cosh(r_1\xi) + b_3 \sinh(r_2\xi) + b_4 \cosh(r_2\xi) \\ & + b_5 \sin(r_3\xi) + b_6 \cos(r_3\xi).\end{aligned} \tag{16}$$

Boundary conditions were applied to determine the constants of these equations. These were carried out using MATLAB® software [19] and by solving the expanded equations numerically or symbolically.

The following boundary conditions were applied for the shear-stress equation:

- Evaluating Equation (3) at both ends of the overlap joint ($\xi = 0$ and $\xi = 1$).
- Making the derivative of Equation (5) two more times and substituting for peel-stress differentiation from Equation (8), then evaluating it at the overlap ends.
- Making the derivative of Equation (5) three more times and substituting for peel-stress differentiation from Equation (9), then evaluating it at the overlap ends.

- Integrating the second equation in (A2) along the overlap length, which is equal to the net of longitudinal applied force,

$$\int_0^1 \tau_{xy} d\xi = \frac{1}{2L}\left(F_2|_{\xi=1} - F_2|_{\xi=0}\right) = \gamma. \tag{17}$$

A similar procedure applied to the peel-stress equation by using Equations (3) and (8)–(10).

Simplified Solution

The general solution of the stress field was explained in the previous section. In this section, an alternative, simpler approximate solution for the peel- and shear-stress distribution, which are easier to implement, is discussed. Then, the deviation of this approximate solution relative to the general solution is investigated.

If we assume that the effects of transverse deflection on the shear distribution is negligible, then the peel stress in Equation (5) can be ignored and Equation (5) simplifies to

$$\frac{d^3\tau_{xy}}{d\xi^3} - k_\tau^2 \frac{d\tau_{xy}}{d\xi} = 0 \tag{18}$$

where k_τ is the same as defined in Equation (13).

The solution of this equation is

$$\tau_{xy} = a_1 \sinh(k_\tau \xi) + a_2 \cosh(k_\tau \xi) + a_3. \tag{19}$$

The following two boundary conditions at either ends of the adhesive layer and Equation (17) were applied to find the constants a_1–a_3.

$$\left.\frac{d\tau_{xy}}{d\xi}\right|_{\xi=0,1} = \frac{G_a n_2 L}{t_a}\left[(F_2 - \phi F_1) - \frac{6}{t_2}\left(M_2 + \frac{\phi t_2}{t_1} M_1\right)\right]_{\xi=0,1} = \begin{Bmatrix} \alpha_0 \\ \alpha_1 \end{Bmatrix}. \tag{20}$$

These constants for dissimilar adherends are as follows:

$$a_1 = \frac{\alpha_0}{k_\tau}, \quad a_2 = \frac{\alpha_1 - \alpha_0 \cosh(k_\tau)}{k_\tau \sinh(k_\tau)}, \quad a_3 = \gamma + \frac{\alpha_0 - \alpha_1}{k_\tau^2}. \tag{21}$$

A simplified solution for the peel-stress distribution was also found by assuming that the shear stress is constant along the overlap length. Then, Equation (10) would be only in terms of the peel stress and the coupling effect is discarded. In fact, from finite element analysis it was found that the shear-stress distribution is nearly uniform and constant along the overlap length away from the overlap ends. Hence,

this is a reasonable assumption. The differential equation governing the peel stress becomes

$$\frac{d^4\sigma_y}{d\xi^4} - 4k_\sigma^4\sigma_y = 0 \tag{22}$$

where k_σ is the same as defined in Equation (13). Equation (22) has the following solution:

$$\begin{aligned}\sigma_y = {} & b_1 \sin(k_\sigma\xi) \sinh(k_\sigma\xi) + b_2 \cos(k_\sigma\xi) \cosh(k_\sigma\xi) \\ & + b_3 \sin(k_\sigma\xi) \cosh(k_\sigma\xi) + b_4 \cos(k_\sigma\xi) \sinh(k_\sigma\xi).\end{aligned} \tag{23}$$

Evaluating Equations (8) and (9) at either ends of the overlap produces four equations to find the constants b_1–b_4. These equations were solved simultaneously by the symbolic toolbox of MATLAB and the results are presented in Appendix B.

CRACK CLOSURE INTEGRAL (CCI)

The stress field is now known according to the equations derived in the previous section. The fracture mechanics parameters can be easily estimated if the energy-release rate, G, can be expressed in terms of stress values at the crack tip. Consider the strain energy-release rate (SERR) when a crack grows an amount Δa; that is, the crack advances from state (a) to state (b) as shown in Figure 3. In this situation, the

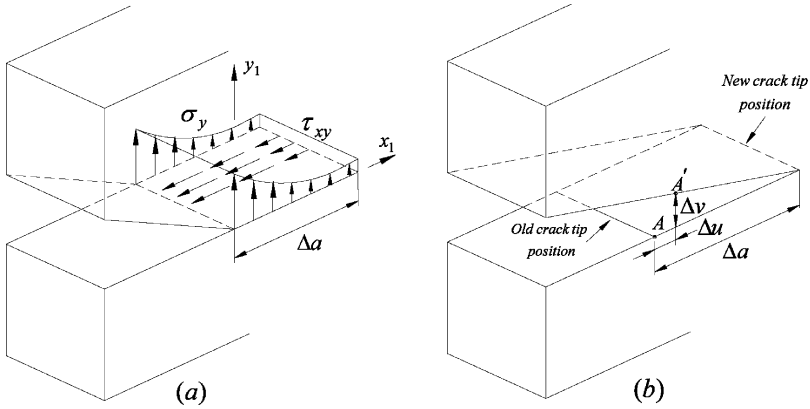

FIGURE 3 Schematic view of crack growth from state (a) at crack increment a to state (b) with crack increment $a + \Delta a$.

shear and peel stresses relax from some value to zero over the crack advance increment Δa, while the crack tip moves from A to A' by Δu and Δv in the x and y directions, respectively. The former change in displacement is caused by the normal stress component, which contributes to Mode I fracture, whereas the latter one is due to the shear-stress component and contributes to Mode II fracture. Alternatively, the result would be the same if we consider the work required to close the crack an amount Δa. The energy-release rate per unit thickness over this crack growth can be written as

$$G\Delta a = \frac{1}{2}\int_0^{\Delta a} \left(\tau_{xy}\Delta u + \sigma_y \Delta \mathrm{v}\right) dx_1. \tag{24}$$

The SERR can be computed from Equation (24) by dividing both sides by Δa and letting $\Delta a \to 0$ (note that stresses are maximum at either ends of overlap according to the derived equations). The variation in displacement is the relative displacement of the two adherends (see Figure 3); therefore, Equation (24) can be rearranged as

$$G = 0.5\hat{\tau}\ (u_2 - u_1) + 0.5\hat{\sigma}\ (\mathrm{v}_2 - \mathrm{v}_1) \tag{25}$$

where $\hat{\tau}$ and $\hat{\sigma}$ are shear and peel stresses at the crack tip. Substituting for displacements from Equations (1) and (7) yields

$$G_I = \frac{t_a}{2E_a}\hat{\sigma}^2, \qquad G_{II} = \frac{t_a}{2G_a}\hat{\tau}^2, \tag{26}$$

and the total strain energy-release rate is $G = G_I + G_{II}$.

For linear elastic materials, a simplified relationship between the energy-release rate, G, and stress-intensity factor, K, can be presented as

$$G = \frac{(1-\nu_a^2)}{E_a}\left(K_I^2 + K_{II}^2\right). \tag{27}$$

For the DLJ specimens, it was determined that the failure mechanism was mixed mode. For the present, therefore, no attempt is made to differentiate between the two modes but rather to determine the total fracture energy-release rate, G, to compare it with the experimental values.

J-INTEGRAL METHOD

In this section, the J-integral approach is implemented to calculate fracture parameters and, unlike the CCI method, it can be applied to nonlinear elastic behavior. This integral can be written for the

problem under consideration as

$$J = \oint_{\Gamma} \left[W(\varepsilon) n_1 - \sigma_{ij} n_j \frac{\partial U_i}{\partial x} \right] ds \tag{28}$$

where Γ is a closed contour that encloses the crack tip and part of the adhesive layer over the bonded lap, W is the strain energy per unit volume, n_j is the direction cosine of the outward unit normal vector to Γ, and $U(u,v)$ is the displacement vector along the contour. This equation can be expanded as

$$J = \oint_{\Gamma} \left[\left(\int_0^{\varepsilon} \sigma_{ij} d\varepsilon_{ij} \right) n_1 - \left(\sigma_x n_1 + \tau_{xy} n_2 \right) \frac{\partial u}{\partial x} - \left(\tau_{xy} n_1 + \sigma_y n_2 \right) \frac{\partial \mathrm{v}}{\partial x} \right] ds. \tag{29}$$

Figure 4 shows the contour along which the line integral was calculated. By definition, there is no traction on the crack faces and also $n_1 = 0$ along contour parts 2 and 3; thus, the line integral is zero on these parts. Along divisions 1, 4, and 6, $n_2 = 0$ and only nonzero stress components contribute to the strain energy density. For contour parts 5 and 7, $n_1 = 0$. Therefore, the nonzero components of the J integral would be

$$J_{1,4} = \int_{-t_a/2}^{t_a/2} \left[\int_0^{\varepsilon_y} \left(\sigma_y d\varepsilon_y \right)_{x=0} \right] dy \quad \text{on } \Gamma_{1,4}, \tag{30}$$

$$J_5 = \int_0^{a+\Delta a} \left(\tau_{xy} \frac{\partial u}{\partial x} + \sigma_y \frac{\partial \mathrm{v}}{\partial x} \right) dx \quad \text{on } \Gamma_5, \tag{31}$$

$$J_6 = \int_{-t_a/2}^{t_a/2} \left[\int_0^{\varepsilon} \left(\sigma_y d\varepsilon_y + 2\tau_{xy} d\varepsilon_{xy} \right)_{x=a+\Delta a} \right] dy \quad \text{on } \Gamma_6, \tag{32}$$

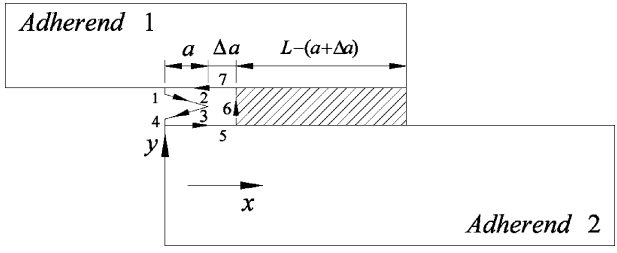

FIGURE 4 Description of the J-integral contour around the crack in the adhesive layer region.

and

$$J_7 = -\int_0^{a+\Delta a} \left(\tau_{xy} \frac{\partial u}{\partial x} + \sigma_y \frac{\partial \mathrm{v}}{\partial x} \right) dx \quad \text{on } \Gamma_7. \tag{33}$$

Equations (30) and (32) should be integrated over the adhesive thickness. Because the adhesive layer is thin, it is reasonable to assume that the variation in stresses in the normal direction across the adhesive layer is negligible. Hence, the J integral on divisions 1, 4, and 6 can be ignored. Therefore, the J integral results from adding Equations (31) and (33), noting that displacements on division 7 are due to adherend 1 and displacements along division 5 belong to adherend 2:

$$J = \int_0^{a+\Delta a} \left[\tau_{xy} \left(\frac{\partial u_2}{\partial x} - \frac{\partial u_1}{\partial x} \right) + \sigma_y \left(\frac{\partial \mathrm{v}_2}{\partial x} - \frac{\partial \mathrm{v}_1}{\partial x} \right) \right] dx. \tag{34}$$

Differentiating Equations (1) and (7) and then substituting for displacement differences leads to

$$J = \int_0^{a+\Delta a} \left(\frac{t_a}{G_a} \tau_{xy} \frac{d\tau_{xy}}{dx} + \frac{t_a}{E_a} \sigma_y \frac{d\sigma_y}{dx} \right) dx. \tag{35}$$

Noting that when the crack grows, stresses are relaxed, and because the adhesive layer is thin, the stress field at the region between $x = 0$ and $x = a$ is negligible. Thus, the lower bound of the integral can be replaced by a. Now, if $\Delta a \to 0$, the shear and peel stresses have values at the crack tip of $\hat{\tau}$ and $\hat{\sigma}$, respectively, and then

$$J = \frac{t_a}{2G_a} \hat{\tau}^2 + \frac{t_a}{2E_a} \hat{\sigma}^2. \tag{36}$$

The J-integral approach resulted in the same relationship as was achieved from the CCI in Equation (26).

NUMERICAL SOLUTION

The finite element (FE) model of the DLJ was considered as consisting of two isotropic, homogeneous and linear–elastic materials joined together along interfaces, as shown in Figure 1. Because of symmetry, only one half of the DLJ was modeled under a plane strain assumption. It should be noted that the analytical model described cannot distinguish between crack growth cohesively through the center of the adhesive layer and crack growth at the adhesive/substrate interfaces. However, the FE approach can obviously model either a cohesive or an

interfacial crack. The analysis was undertaken using ABAQUS software [20].

The *J*-integral method was used to calculate values of *G* as a function of the crack length, *a*. Smelser and Gurtin [21] have shown that the *J* integral for a nonhomogeneous solid composed of dissimilar materials is the same as the analogous result for a single-phase material. Thus, for an interfacial crack problem, the line integral has the same form as the well-known *J*-integral for monolithic solids, provided the surfaces are free from traction and the interface is a straight line.

For a quasi-static crack advance, two methods are typically used for calculating the *J* integral in a two-dimensional analysis. One method is based on a line-integral expression and the other method uses the divergence theorem, where the contour integral can be expanded into an area integral over a finite domain that surrounds the crack tip. In FEA, coordinates and displacements refer to nodal points and stresses and strain refers to the Gaussian integration point. Hence, it is more convenient to evaluate the contour integral using the domain integral and this method is used in ABAQUS. The number of different evaluations of *J* possible is the number of such rings of elements.

For small scale and contained yielding, a path-independent integral can be computed outside the plastic zone. This means that the *J* contour has to be large enough to surround the plastic zone and pass through the elastic region only. However, in a blunting crack case, significant stress redistribution occurs at the crack tip and the path dependence increases strongly. Also, as the stress singularity at the blunting crack tip vanishes under the assumption of finite strains and incremental plasticity, *J* will not have a finite value any more. This is because the work dissipated by plastic deformation should always be positive and the calculated *J* values have to increase monotically with the size of the domain, except for the contour that touches the domain boundaries. For these cases, the highest calculated *J* value with increasing domain size in the far-field remote from the crack tip is always the closest to the real far-field *J*. Accurate estimates of the contour integral are usually determined even with quite coarse meshes.

In the elastic analysis, the cracks were assumed to be sharp, and the crack faces were assumed to lie on top of one another in the undeformed configuration. These types of cracks are normally analyzed under small-strain assumptions, as the strain field is singular at the crack tip and this singular zone is localized. The variations in the estimates of the *J* integral from domain rings, excluding the crack tip itself, were very small. The present FE modeling was performed

TABLE 1 Properties of Double Lap Joint Specimens

	Adherend 1–steel	Adherend 2–steel	Adhesive
Young's modulus, E (GPa)	207	207	4
Poisson's ratio, ν	0.3	0.3	0.38
Thickness, t (mm)	6	12	1
Yield stress (MPa)	350	350	35

assuming linear–elastic behavior. Material properties used in the FEA are summarized in Table 1. In the present work, four-noded isoparametric elements were used for the whole domain. A typical model of the joint was composed of 10,000 elements and 10,431 nodes (see Figure 5). A range of crack lengths were used in the model and the crack was positioned at the point A or D of the geometry as shown in Figures 1 and 5. The results for the stress analysis are presented in a later section. Also, the displacements measured between positions A and D in Figure 5 are used to derive the compliance for different crack lengths to compare with the experimental values measured at the same positions as described in the next section.

EXPERIMENTS

The substrates used throughout the present article were prepared from a 316 stainless steel and were bonded by using a hot-curing

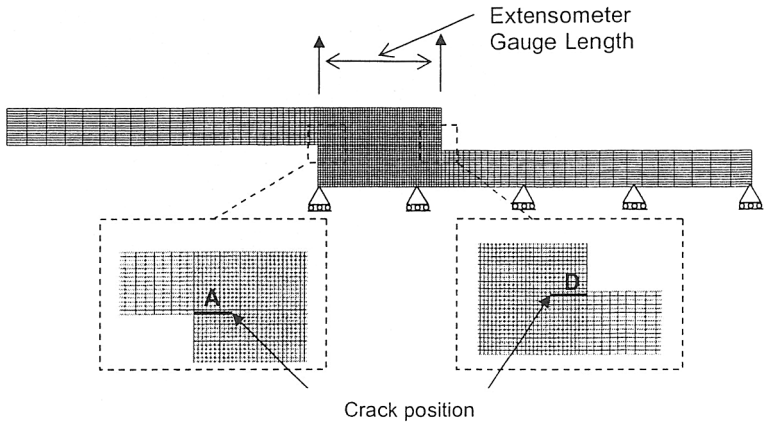

FIGURE 5 Finite element mesh for the half section of the double lap joint (DLJ) specimen.

toughened-epoxy adhesive ESP110 (Permabond Eastleigh, UK). Prior to bonding, the steel substrates were pretreated using a grit-blast and degrease (GBD) treatment. For these joints, the substrates were first washed with water to remove any gross contamination, after which they were degreased with acetone. The substrates were lightly grit-blasted with alumina grit and any grit was removed with compressed air. They were then cleaned with acetone, washed in cold tap water, and dried prior to being bonded.

The double lap joint specimens (shown schematically in Figure 1) were made from two outer 6-mm stainless steel plates and an inner 12-mm stainless steel plate with the width of $w = 20$ mm. After the steel plates were pretreated, they were bonded with an overlap length of $L = 20$ mm. The bonded plates were held together using clips while they were cured for 60 min at 180°C. The specimens were then allowed to cool in the oven, during which procedure naturally occurring spew fillets of adhesive formed at the ends of the overlap. Different sizes of precracks were inserted at point A and point D and the symmetrical location is shown in Figure 1 of both bondlines where a thin sheet of PTFE had been inserted prior to curing.

The specimens were tested under monotonic tensile-loading conditions. The joints were loaded using a constant displacement rate of 1 mm/min in a "dry" environment at room temperature and failed under tensile applied loads, P, to different failure loads of P_f. The failure loads of the double lap joint with different precrack lengths for position A and D are summarized in Table 2. The displacement was measured both with an extensometer placed between positions

TABLE 2 Failure Load and Fracture Energy of DLJ Specimen Derived from Experimental, Analytical, and Numerical Calculations for Different Crack Length

	Crack at position D				Crack at position A			
	Experiments		Analytical	FEA	Experiments		Analytical	FEA
Crack length (mm)	Failure load, P_f (kN)	G_f (J/m^2)	G_f (J/m^2)	G_f (J/m^2)	Failure load, P_f (kN)	G_f (J/m^2)	G_f (J/m^2)	G_f (J/m^2)
0	33.9	—	—	—	36.5	—	—	—
2	28.2	662	823	750	34.2	600	983	870
4	24.6	688	944	732	32	841	1143	930
6	20.8	694	741	691	27.6	937	954	920
8	17.2	660	762	640	23	915	942	855
10	15.1	689	730	683	17.1	680	748	660
12	12.2	591	699	626	14.2	603	745	670

A and D as shown in Figure 5 and remotely between the grips using the testing machine displacement recorder. The local displacement measurements between A and D were used to derive the compliance for different crack lengths and crack positions. An example of the load displacement measured locally with an extensometer and globally using the machine displacement for a precrack length of 8 mm are shown in Figure 6. It is clear that the appropriate displacement measurement needed for the analysis is the local one and not the global displacement, which is not representative of the deformation local to the bondline interface.

Figure 7 compares the experimental DLJ compliance measurements and the results from FE calculations. The FE compliance is shown to be slightly different between specimens with cracks at side A and D. The difference is larger for longer crack length. Essentially where the tensile peel stresses are higher at position D, the

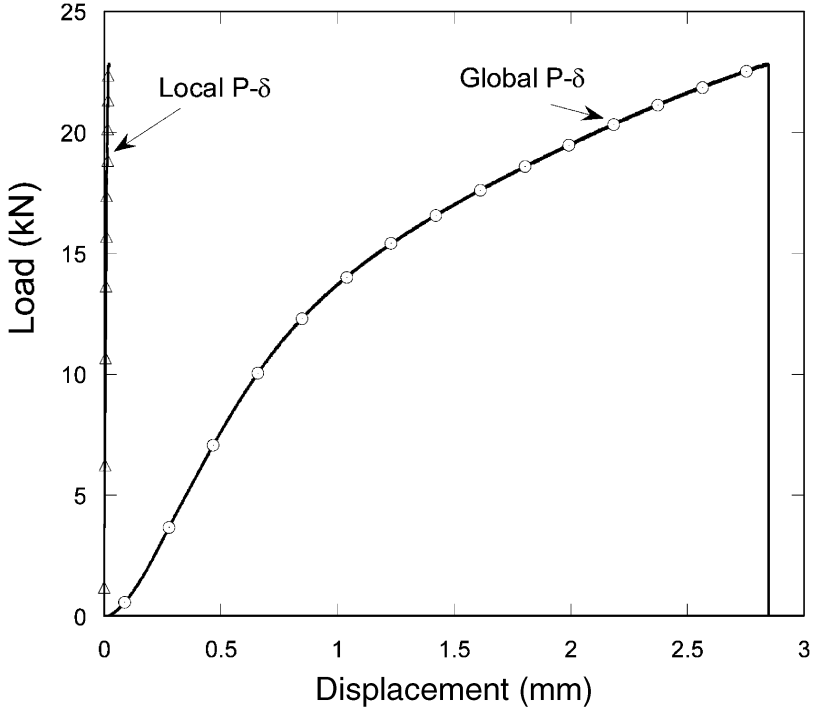

FIGURE 6 Local and global load-displacement curve of an epoxy-bonded DLJ specimen tested under monotonic load at a crack length of 8 mm for a crack at the left-hand side A (see Table 2).

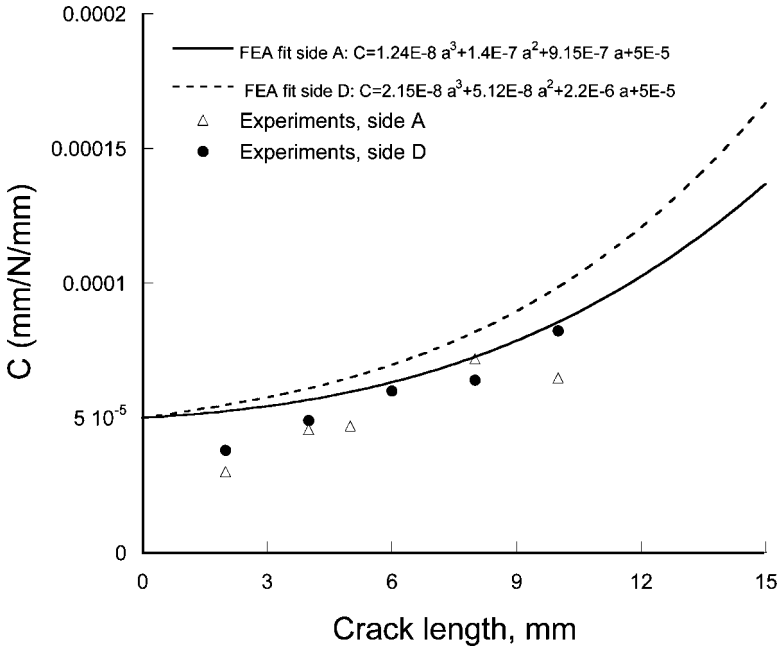

FIGURE 7 Comparison of DLJ compliance measured from experiments and obtained from FEA.

compliance tends to be larger when compared with cracks at position A. The agreement is reasonable, with the experimental results falling slightly lower than the FE calculations, hence making the FE compliance a conservative estimate. Using the FE results, the compliance of the DLJ can be described as a function of crack length by

$$C = \delta/p = f(a) \tag{37}$$

where $p = P/2w$ and

$$f(a) = 1.24 \times 10^{-8}a^3 + 1.4 \times 10^{-7}a^2 + 9.15 \times 10^{-7}a + 5 \times 10^{-5} \text{ (Side A)},$$
$$f(a) = 2.15 \times 10^{-8}a^3 + 5.1 \times 10^{-8}a^2 + 2.2 \times 10^{-6}a + 5 \times 10^{-5} \text{ (Side D)}. \tag{38}$$

In these, the dimension of p is in N/mm and δ is in mm. The experimental fracture energy was then calculated from the measured failure load per unit width per arm, $p_f = P_f/2w$, by

$$G = \frac{p_f^2}{2}\frac{dC}{da} \tag{39}$$

where

$$\frac{dC}{da} = 3.72 \times 10^{-8} a^2 + 2.8 \times 10^{-7} a + 9.15 \times 10^{-7} \text{ (Side A)},$$
$$\frac{dC}{da} = 6.45 \times 10^{-8} a^2 + 1.02 \times 10^{-7} a + 2.2 \times 10^{-6} \text{ (Side D)}. \quad (40)$$

The results of experimental failure load and fracture energy are presented in Table 2. The locus of failure was found to be a mixture of interfacial (visually) and cohesive fracture for all joints.

COMPARISON OF ANALYTICAL AND NUMERICAL RESULTS

Several examples were solved to show the accuracy of the analytical solution in comparison with the numerical analysis. Both stress distributions and fracture parameters were obtained. Comparisons with experimental data were made in some cases. The importance of shear- and peel-stress components can be judged from the results and decisions can be made whether to use the general solution or the simplified one. The shear and peel stresses were normalized by multiplying them by the factor (t_2/F_2^x). A sample of a contour plot of shear- and peel-stress distribution in DLJ from FEA is shown in Figure 8 for crack positions A and D.

In the first example, a DLJ without any crack was considered. The joint was under tensile loading of $F_2^x = 2F_1^x = 600\,\text{N/mm}$. Figure 9 compares the shear-stress distribution along the interface of adhesive and adherend 2 obtained from numerical and analytical solutions. Both general and simplified solutions are shown. The analytical solution shows good agreement with finite element results and the general solution generally gives a more accurate representation. Some discrepancies can be seen at the overlap ends. In fact, these spots act like singular points and the finite element method tries to model the zero stress state at traction-free end surfaces. The difference between stress distribution from analytical and FEA solutions along the overlap and away from its ends is negligible. In Figure 10 peel-stress distribution resulting from simplified analytical and FEA solutions along the interface CD in an uncracked DLJ are compared. Again, the analytical solution agrees quite well with the FEA results.

Figure 11 shows the effect of the crack length on the shear-stress distribution obtained from the general solution and the FEA. Two different crack lengths of 2 mm and 5 mm at position A were considered on one side of the bondline (as shown in Figures 1 and 5) and the stress distribution was plotted along the cracked side of the adhesive.

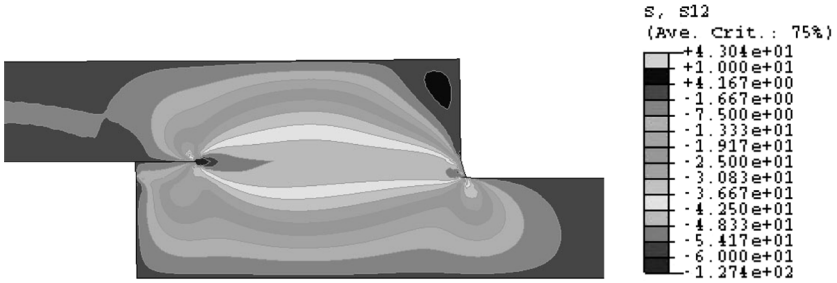

(a) Shear-stress crack at side A

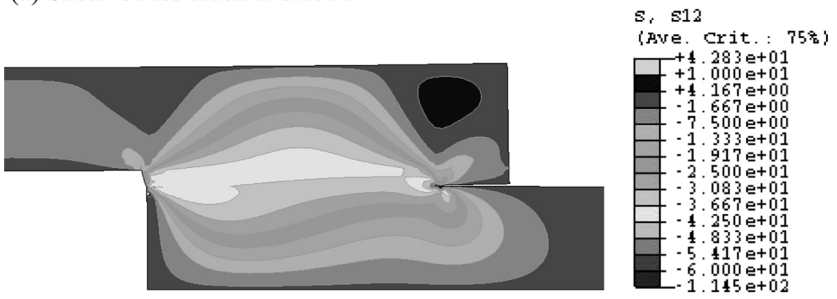

(b) Shear-stress crack at side D

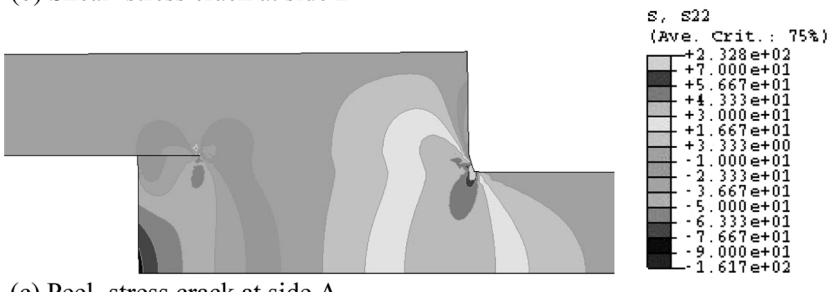

(c) Peel-stress crack at side A

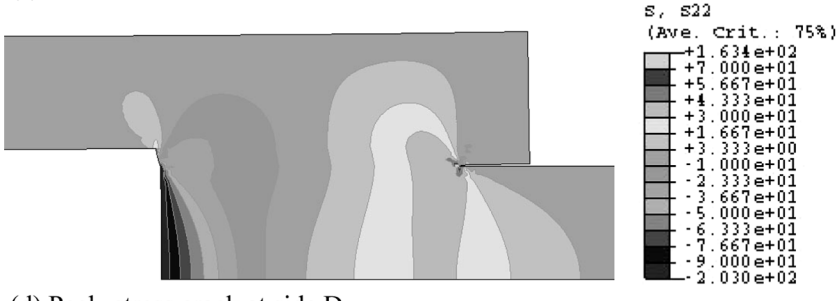

(d) Peel-stress crack at side D

FIGURE 8 Distribution of peel stress and shear stress along the bonded part of DLJ at a crack length of 4 mm with the crack placed either at side D or at side A.

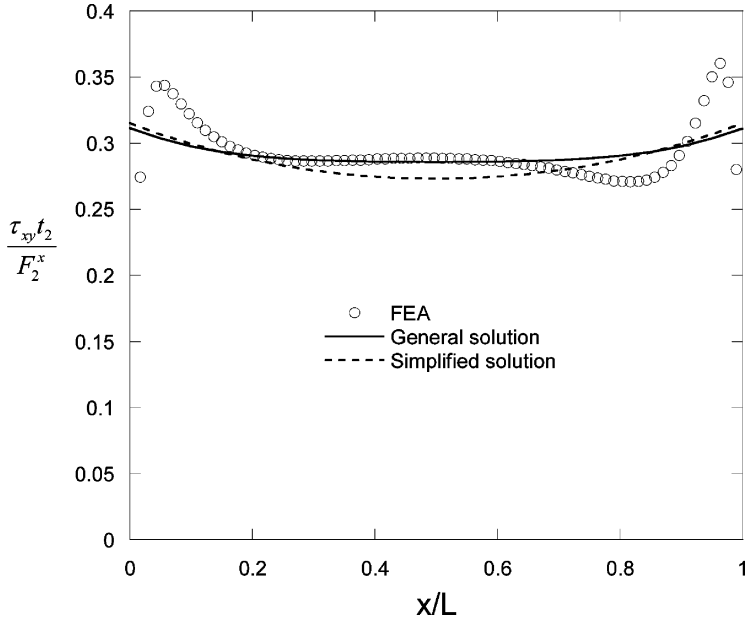

FIGURE 9 Distribution of shear stress along the interface CD between adhesive and adherend 2 (uncracked DLJ).

In Figure 12, a similar comparison between peel stress computed from the simplified solution and the FEA for the same crack lengths is made. In all cases, the agreement between analytical solution and FEA was generally acceptable except in the vicinity of the crack tip.

COMPARISON WITH EXPERIMENTAL RESULTS

The peel-stress contours at the crack tips in Figures 8c and d suggest that the specimen is subjected to mixed-mode loading, although Mode I seems to be dominant. It is also observed that the tensile peel stresses at position D cause crack opening, while the compressive peel stress at position A causes crack closure. Therefore, the fracture energy depends on crack position.

For each experimental case shown in Table 2, the specific values of the strain energy-release rate, G_f, from the experiments, FEA J integrals, and the analytical calculations were derived and compared. Figure 13 compares the strain energy-release rates with the fracture computed for each test case *versus* the normalized crack length, a/L. The experimental, analytical, and numerical solutions for G_f show a very good overall agreement. The increased discrepancy at the shorter

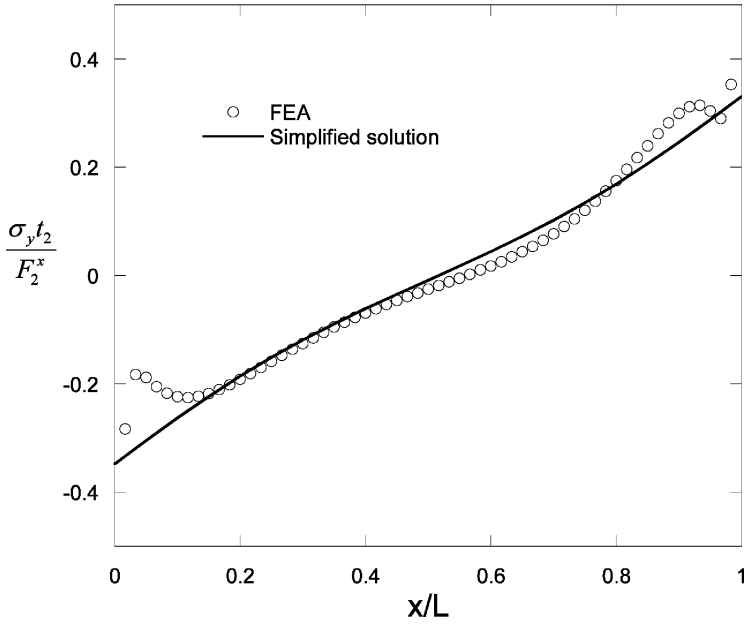

FIGURE 10 Distribution of peel stress along the interface CD between adhesive and adherend 2 (uncracked DLJ).

crack length is due to the increased experimental scatter. Errors resulting from the exact fabrication of the specimen, such as in controlling the initial crack size and the thickness of the adhesive layer contribute to the scatter. However, it is shown in Figure 13 that the best-fit mean value of G_f is relatively constant with respect to crack length except at the very long crack lengths. It is also evident that the mean experimental strain energy-release rate for specimens at position D is lower by about 20% when compared with specimens with cracks at position A.

CONCLUSIONS

A general analytical solution has been presented to estimate the shear and peel stresses along the bonded layer of double-lap joints and to calculate the fracture energy of the adhesive. By assuming that the transverse deflection on the shear distribution is negligible, the general solution was further simplified. It was shown that the simplified solution is sufficient for deriving the peel stress but to obtain more precise results for the shear stress, the general solution gives a more accurate answer. Using the stress field from the analytical solution,

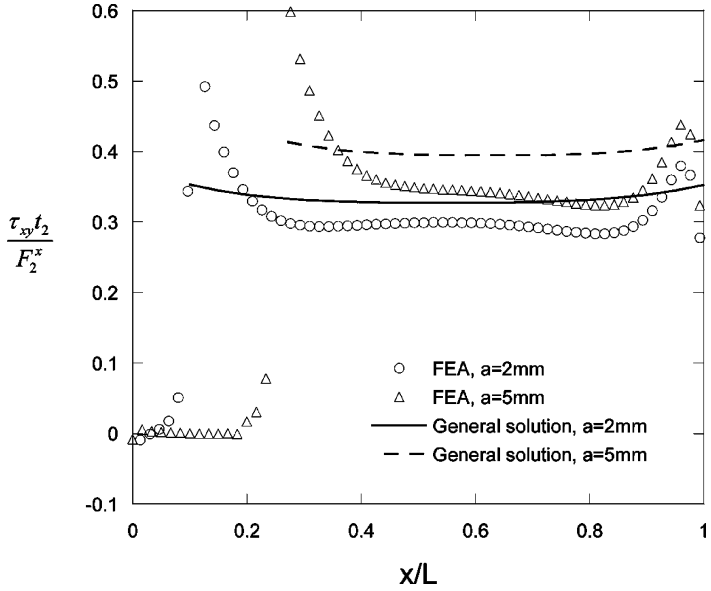

FIGURE 11 Shear-stress profile at two different crack lengths at point C along the bondline of adherend 2.

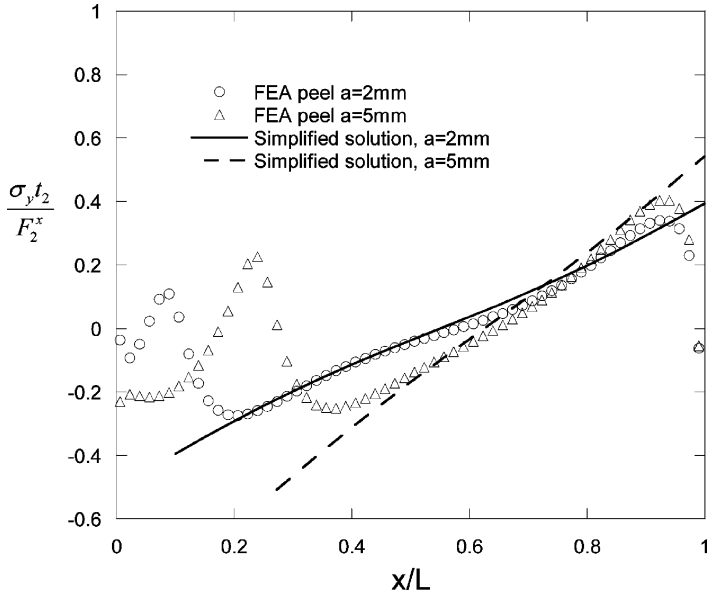

FIGURE 12 Peel-stress profile at two different crack lengths at point C along the bondline of adherend 1.

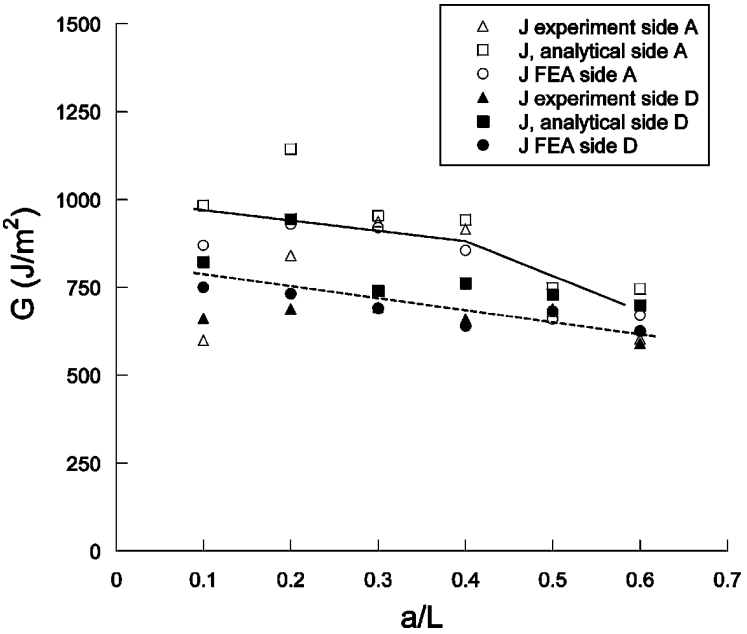

FIGURE 13 Comparisons of energy-release rate at failure, G_f, with crack length using experimental, numerical, and analytical solutions to derive G. Solid markers are for a crack at side A, and open markers are for a crack at side D.

the adhesive fracture energy was calculated in two ways. This was done either by using the crack closure integral (CCI) or by means of the J-integral approach. Furthermore, the calculated fracture energy from the analytical solutions was verified by the J integral obtained from finite element analysis. The tests carried out contained cracks at different ends of the DLJ. The loading was determined to be mixed-mode at the crack tip for this particular geometry. In addition, the experimentally measured local compliance (displacement/load) of the adhesive compared well with that derived from the FE and was found to be slightly lower than the predicted FE values. The calculated values of G_f at failure, from the limited number of tests performed, compared reasonably well with the analytical and numerical derivations for G. The fracture energy results for the adhesive used in the DLJ specimens showed relative independence with respect to crack length. However, the fracture energy for the crack starter in the position where the peel stress was found to be tensile was approximately 20% lower than for the tests where the crack was positioned at the side, where the peel stress was shown to be compressive.

ACKNOWLEDGMENT

The authors thank A. Nyilas of Forschungszentrum Karlsruhe, Germany, for his help and advice.

REFERENCES

[1] Volkersen, O., *Luftfahrtforschung* **15**, 41–47 (1938).
[2] Goland, M. and Reissner, E., *J. Appl. Mech.* **11**, A17–A24 (1944).
[3] Hart-Smith, L. J., Technical Report NASA CR 112235, Douglas Aircraft Company (1973).
[4] Hart-Smith, L. J., Technical Report NASA CR 112236, Douglas Aircraft Company, (1973).
[5] Hart-Smith, L. J., Technical Report NASA CR 112237, Douglas Aircraft Company, (1973).
[6] Williams, J. G., *Int. J. Fract.* **36**, 101–119 (1988).
[7] Kinloch, A. J., *Adhesion and Adhesives: Science and Technology* (Chapman and Hall, London, 1987).
[8] Hamoush, S. A. and Ahmad, S. H., *Int. J. Adhes. Adhes.* **9**, 171–178 (1989).
[9] Bigwood, D. A. and Crocombe, A. D., *Int. J. Adhes. Adhes.* **9**, 229–242 (1989).
[10] Fernlund, G., Spelt, J. K., *Engng. Fract. Mech.* **40**, 119–132 (1991).
[11] Edde, F. and Verreman, Y., *Int. J. Adhes. Adhes.* **12**, 43–48 (1992).
[12] Chiu, W. K. and Jones, R., *Int. J. Adhes. Adhes.* **12**, 219–225 (1992).
[13] Williams, J. G., *J. Strain Analysis* **28**, 237–246 (1993).
[14] Hadavinia, H., Kinloch, A. J., Little, M. S. G., and Taylor, A. C., *Int. J. Adhes. Adhes.* **23**(6), 463–471 (2003).
[15] Lee, K. J., *Comput. Struct.* **56**, 637–643 (1995).
[16] Her, S. C., *J. Comp. Struct.* **47**, 673–678 (1999).
[17] Pereira, A. B. and Morais, A. B. *Int. J. Adhes. Adhes.* **23**, 315–322 (2003).
[18] Dym, C. L. and Shames, I. H., *Solid Mechanics: A Variational Approach* (McGraw-Hill, New York, 1973).
[19] Hunt, B., Lipsman, R., and Rosenberg, G., *A guide to MATLAB* (Cambridge University press, Cambridge, 2001).
[20] Hibbitt, Karlsson & Sorensen, Inc., USA, ABAQUS/CAE version 6.2 (2001).
[21] Smelser, R. E. and Gurtin, M. E., *Int. J. Fract.* **13**, 382–384 (1977).

APPENDIX A

The force and moment equilibrium equations for a differential element, dx, within the joint can be written as follows (see Figure 2):

$$\begin{cases} \dfrac{dQ_1}{dx} = -\sigma_y \\ \dfrac{dF_1}{dx} = -\tau_{xy} \\ \dfrac{dM_1}{dx} = Q_1 - \dfrac{t_1}{2}\tau_{xy}, \end{cases} \tag{A1}$$

$$\begin{cases} \dfrac{dQ_2}{dx} = 0 \\ \dfrac{dF_2}{dx} = 2\tau_{xy} \\ \dfrac{dM_2}{dx} = Q_2 \end{cases} \tag{A2}$$

where subscripts 1 and 2 stand for the outer and the inner adherends, respectively. The equations were derived for a unit width in the z direction.

APPENDIX B

The right-hand sides of Equations (8) and (9) were evaluated at either ends of the bonded region to calculate the constants of Equation (23) as

$$\frac{E_f L^2}{2t_a D_2 k_\sigma^2}(M_2 - fM_1) = \begin{cases} T_1 & at \quad \xi = 0 \\ T_2 & at \quad \xi = 1, \end{cases} \tag{B1}$$

$$\left(Q_2 - fQ_1 + \frac{ft_1}{2}\tau_{xy}\right)\frac{L^3}{2k_\sigma^3} = \begin{cases} T_3 & at \quad \xi = 0 \\ T_4 & at \quad \xi = 1, \end{cases} \tag{B2}$$

then the second and third differentiations of Equation (23) were also evaluated at these geometrical points to develop a relation between the b_1–b_4 coefficients and Equations (B1) and (B2). The solution of this system of equations would be as follows:

$$\begin{aligned} b_1 &= T_1/s_4, \\ b_2 &= \{T_1(s_1^4 + 4s_1^2 s_2 s_3 - 1) + 2T_2[s_1(s_3 - s_2) - s_1^3(s_3 + s_2)] \\ &\quad + 4T_3 s_1^2 s_2^2 + 2T_4 s_2(s_1^3 - s_1)\}/s_4, \\ b_3 &= \{-T_1[(s_1^2 - 1)^2 + 4s_1^2 s_2^2] + 4T_2 s_2(s_1^3 - s_1) \\ &\quad + T_3(-s_1^4 + 4s_1^2 s_2 s_3 + 1) \\ &\quad + 2T_4[s_1^3(s_3 - s_2) - s_1(s_3 + s_2)]\}/s_4, \\ b_4 &= \{T_1(s_1^4 + 4s_1^2 s_2 s_3 - 1) + 2T_2[s_1(s_3 - s_2) - s_1^3(s_3 + s_2)] \\ &\quad + T_3(s_1^4 - 2s_1^2 + 1) + 2T_4 s_2(s_1^3 - s_1)\}/s_4, \end{aligned} \tag{B3}$$

in which

$$s_1 = \exp(k_\sigma), \quad s_2 = \sin(k_\sigma), \quad s_3 = \cos(k_\sigma) \tag{B4}$$

$$s_4 = 4s_1^2 s_2^2 - (s_1^2 - 1)^2. \tag{B5}$$